Carbohydrate Polymers 337 (2024) 122156

Contents lists available at ScienceDirect

Carbohydrate Polymers

journal homepage: www.elsevier.com/locate/carbpol

Seaweed-derived fucoidans and rhamnan sulfates serve as potent anti-SARS-CoV-2 agents with potential for prophylaxis

Yuefan Song [a], Amit Singh [b], Maisha M. Feroz [a,c], Shirley Xu [a,c], Fuming Zhang [a,c], Weihua Jin [d], Ambrish Kumar [e], Parastoo Azadi [e], Dennis W. Metzger [a,b], Robert J. Linhardt [a,c,f,g], Jonathan S. Dordick [a,c,g,h,*]

[a] Center for Biotechnology & Interdisciplinary Studies, Rensselaer Polytechnic Institute, Troy, NY 12180, United States of America
[b] Department of Immunology and Microbial Disease, Albany Medical College, Albany, NY 12208, United States of America
[c] Department of Chemical and Biological Engineering, Rensselaer Polytechnic Institute, Troy, NY 12180, United States of America
[d] College of Biotechnology and Bioengineering, Zheijiang University of Technology, Hangzhou 310014, China
[e] Complex Carbohydrate Research Center, University of Georgia, Athens, GA 30602, United States of America
[f] Department of Chemistry and Chemical Biology, Rensselaer Polytechnic Institute, Troy, NY 12180, United States of America
[g] Department of Biological Sciences, Rensselaer Polytechnic Institute, Troy, NY 12180, United States of America
[h] Department of Biomedical Engineering, Rensselaer Polytechnic Institute, Troy, NY 12180, United States of America

ARTICLE INFO

Keywords:
Fucoidan
Rhamnan sulfate
SARS-CoV-2
Fractionation
In vitro anti-SARS-CoV-2 activity
In vivo prophylaxis

ABSTRACT

Seaweeds represent a rich source of sulfated polysaccharides with similarity to heparan sulfate, a facilitator of myriad virus host cell attachment. For this reason, attention has been drawn to their antiviral activity, including the potential for anti-SARS-CoV-2 activity. We have identified and structurally characterized several fucoidan extracts, including those from different species of brown macroalga, and a rhamnan sulfate from a green macroalga species. A high molecular weight fucoidan extracted from *Saccharina japonica* (FS*j*RPI-27), and a rhamnan sulfate extracted from *Monostroma nitidum* (RS*Mn*), showed potent competitive inhibition of spike glycoprotein receptor binding to a heparin-coated SPR chip. This inhibition was also observed in cell-based assays using hACE2 HEK-293 T cells infected by pseudotyped SARS-CoV-2 virus with IC_{50} values <1 μg/mL. Effectiveness was demonstrated *in vivo* using hACE2–transgenic mice. Intranasal administration of FS*j*RPI-27 showed protection when dosed 6 h prior to and at infection, and then every 2 days post-infection, with 100 % survival and no toxicity at 10^4 plaque-forming units per mouse *vs.* buffer control. At 5-fold higher virus dose, FS*j*RPI-27 reduced mortality and yielded reduced viral titers in bronchioalveolar fluid and lung homogenates *vs.* buffer control. These findings suggest the potential application of seaweed-based sulfated polysaccharides as promising anti-SARS-CoV-2 prophylactics.

1. Introduction

Algae allocate a significant portion of their organic carbon (up to 80 %) into polysaccharides (Bligh et al., 2022). In marine macro-algae, these polysaccharides serve various roles, from impacting microbial communities (Yu et al., 2024) to intracellular storage and key components of the cell wall and extracellular matrix (ECM). For example, brown seaweeds store laminarin, a water-soluble glucan, in cellular vacuoles, and contains other glycans, including alginates and cellulose within their cell walls and ECM (Bligh et al., 2022; Stiger-Pouvreau et al., 2016). Another class of algal polysaccharides are the heteropolysaccharides containing a high degree of sulfation. These include the fucoidans from brown algae, rhamnan sulfates from green algae, and carrageenan from red algae. These sulfated glycans have attracted significant attention due to their demonstrated biological activity and unique rheological and gelling properties (Beaumont et al., 2021).

Fucoidans are highly fucosylated polysaccharides comprised of fucose pyranose (Fucp), galactose, mannose, xylose, glucose, and glucuronic acid within a highly branched network (Ale et al., 2011; Song et al., 2018; Yuguchi et al., 2016). Fucoidans are largely composed of α-(1 → 3)-L-Fucp residues or alternating α-(1 → 3) and α-(1 → 4)-linked

* Corresponding author at: Center for Biotechnology & Interdisciplinary Studies, Rensselaer Polytechnic Institute, Troy, NY 12180, United States of America.
E-mail address: dordick@rpi.edu (J.S. Dordick).

https://doi.org/10.1016/j.carbpol.2024.122156
Received 4 January 2024; Received in revised form 9 April 2024; Accepted 10 April 2024
Available online 16 April 2024

L-Fucp in the polysaccharide backbone (Wang, Huang, et al., 2020). In addition, α-(1 → 2)-L-Fucp residues are present (Duarte et al., 2001; Song et al., 2018) and a linear core of galactan with branched chains of fucans has been suggested (Duarte et al., 2001; Hanisch, 2023). Sulfate groups can be present at the C-2, C-3, and C-4 positions, and acetyl groups also can be present (Duarte et al., 2001; Song et al., 2018; Wang, Huang, et al., 2020). Fucoidans possess a broad array of biological activities, including anticoagulant (Yao & Yim, 2021), antitumor (Cao et al., 2021; Oliveira et al., 2020), immunomodulatory (Apostolova et al., 2020), hypolipidemic (Peng et al., 2018), hepatoprotective (Song et al., 2017), and antiviral activities (Luthuli et al., 2019).

The green algae-derived rhamnan sulfates are branched polysaccharides consisting primarily of rhamnose pyranose (Rhap), with minor monosaccharides including xylose, glucose, and glucuronic acid (Lee et al., 2010). The typical backbone of rhamnan sulfate consists of →3)-α-L-Rhap-(1 → and →2)-α-L-Rhap-(1 → residues, and the presence of →2,3)-α-L-Rhap-(1 → residues confirm its branching (Lee et al., 2010). The sulfate groups are believed to be located at C-2, C-3, and C-4 (Wang, Wang, et al., 2020). Similar to fucoidans, rhamnan sulfates have been reported to exhibit a wide range of biological properties, including anticoagulant, antiviral, anti-obesity, and anti-inflammatory activities (Chi et al., 2023).

The antiviral activity of fucoidans, rhamnan sulfates, as well as the red macroalga-derived carrageenans (Álvarez-Viñas et al., 2021) suggests that these polysaccharides may possess structural features that are particularly favorable in blocking viral infectivity, and that such structural features may extend beyond algal polysaccharides. Indeed, heparin, a highly sulfated glycosaminoglycan used as an anticoagulant drug, binds to myriad viral surface proteins by mimicking cell surface heparan sulfate (HS), which acts as a facilitator of infection for a large number of viruses, including SARS-CoV-2, the causative agent of COVID-19, several other coronaviruses, respiratory syncytial virus, Varicella zoster, Vaccinia, and others (Kamhi et al., 2013). In the case of SARS-CoV-2, the binding of viral spike glycoprotein (SGP) to epithelial HS increases the local virus concentration (Bermejo-Jambrina et al., 2021) at the cell surface and positions the virus to the ACE2 receptor for cell entry (Clausen et al., 2020; Kim et al., 2020; Liu et al., 2021; Yue et al., 2021; Zhang et al., 2020), ultimately leading to infection. In addition to glycosaminoglycans (GAGs), the semi-synthetic pentosan polysulfate (PPS), which is used in the treatment of interstitial cystitis (Taneja, 2021), has also been shown to bind to the SGP receptor-binding domain (RBD) (Shi et al., 2022). Both heparin and PPS can inhibit infection of SARS-CoV-2 using *in vitro* binding and cell-based studies (Clausen et al., 2020; Shi et al., 2022).

The effectiveness of heparin and PPS in inhibiting SGP binding and cellular entry, and the demonstrated antiviral activity of fucoidans and rhamnan sulfate, suggests that these sulfated marine polysaccharides also possess anti-SARS-CoV-2 activity (Pradhan et al., 2022; Ray et al., 2022; Salih et al., 2021). Previously, we reported fucoidan extracts from the brown algae, *Saccharina japonica*, had significant anti-SARS-CoV-2 activity *in vitro* (Kwon et al., 2020). Two extracted products, high molecular weight F*Sj*RPI-27 and its lower molecular weight breakdown product, F*Sj*RPI-28, had EC_{50} values of several μg/mL against active SARS-CoV-2 isolated from a COVID-19 patient, thereby demonstrating highly potent antiviral activity. Furthermore, using a series of SGP RBD binding and cell-based pseudovirus infectivity studies, rhamnan sulfate from *Monostroma nitidum* (RS*Mn*) possessed potent anti-SARS-CoV-2 activity *in vitro* (Song et al., 2021).

In the current work, we performed detailed compositional analysis and further fractionation of *S. japonica*-derived F*Sj*RPI-27 and F*Sj*RPI-28, along with crude sulfated polysaccharide extracts from another kelp, *Saccharina latissima*, and RS*Mn*. A series of *in vitro* competition SGP RBD binding studies and cell-based anti-SARS-CoV-2 infectivity studies using pseudovirus particles were performed. We then expanded to *in vivo* studies of active virus intranasal (*i.n.*) infectivity of human ACE2 (hACE2) transgenic mice using F*Sj*RPI-27 as a highly active, model fucoidan. Delivery of F*Sj*RPI-27 *i.n.* was performed to mimic nasal spray dosing prior to, or during, infection, which would be consistent with the hypothesis that F*Sj*RPI-27 may serve as a potential prophylactic against SARS-CoV-2 infection.

2. Materials and methods

2.1. Materials and reagents

A high-molecular-weight fucoidan, F*Sj*RPI-27, and a low molecular-weight fucoidan, F*Sj*RPI-28, were prepared from the brown algae *S. japonica* and were generously provided by Dr. Weihua Jin from Zhejiang University of Technology. F*Sj*RPI-28 is derived from F*Sj*RPI-27 by treating a 1.5 % (*w/v*) aqueous solution of F*Sj*RPI-27 with hydrogen peroxide and ascorbic acid, both at a final concentration of 25 mM, for 2 h at room temperature (RT). Additionally, fucoidan was isolated from the brown algae *S. latissima* provided as ground kelp by the Montauk Seaweed Supply Co. (Montauk, NY). Rhamnan sulfate obtained from an extract of the green algae *M. nitidum* (RS*Mn*) was from Calroy Health Sciences, LLC (Scottsdale, AZ). Porcine heparin was obtained from Smithfield Biosciences (Cincinnati, OH), and pentosan polysulfate (PPS) was obtained from Bene Pharma (Munich, Germany). The SARS-CoV-2 SGP RBD, expressed in Expi293F cells from constructs encoding amino acids R319-K537 of WT spike protein (YP_009724390.1)) was generously provided by Dr. John Bates from University of Mississippi Medical Center. Surface plasmon resonance (SPR) sensor streptavidin (SA) chips were obtained from Cytiva (Uppsala, Sweden). High performance liquid chromatography (HPLC) and mass spectrometry (MS) reagents were of HPLC grade, while all other reagents were of ACS grade.

2.2. Preparation of glycan fractions

Crude extracts from *S. latissima* were generated as follows: the dried kelp was ground and suspended in 10 times its weight of distilled water. The suspension was thoroughly stirred and heated in a water bath at 70 °C for 2 h. After centrifugation at 6000 ×*g*, the supernatant was collected and ethanol was added to the solution at a final concentration of 30 % (*v*/v) ethanol, and the resulting precipitate was removed by centrifugation at 6000 ×*g*. The supernatant was then mixed with ethanol to achieve a final concentration of 70 % (v/v) ethanol, and the resulting precipitate was collected by centrifugation at 6000 ×*g* and labeled as the crude extract from *S. latissima*. For crude extracts from *M. nitidum*, the extract of the algae was re-extracted to remove insoluble components as follows. The powder was mixed with 20-times its weight of distilled water and left overnight at 4 °C. The solution was then heated in a water bath at 70 °C, thoroughly stirred, and centrifuged at 6000 ×*g*. The supernatant was collected, and the residue was extracted again using the same amount of distilled water as described above. The supernatants were combined, dialyzed against water for 48 h using Spectra/Por™ 1000 Da molecular weight cut-off (MWCO) cellulose dialysis tubing (Thomas Scientific, Swedesboro, NJ), and then lyophilized to obtain the crude extract.

The crude extracts from the two macro-algae, as well as the fucoidans RPI-27 and RPI-28, were subjected to a sequential fractionation procedure (Fig. S1). To this end, the crude extracts and F*Sj*RPI-27 and F*Sj*RPI-28 were dissolved in distilled water and subjected to sequential MWCO separation and strong anion-exchange (SAX) fractionation. For the former, the glycan solution was sequentially passed through a series of ultrafiltration steps using 100, 30, 10, and 3 kDa filters (Millipore Sigma, Burlington, MA). Each fraction was collected, freeze-dried, and weighed to calculate isolated yield. Fractions with a recovery of over 14 % were further fractionated using SAX chromatography. Twenty milligrams of the major fractions were dissolved in 0.2 M NaCl and loaded onto a Vivapure® D Maxi H column (Sartorius, Göttingen, Germany). Elution was performed sequentially using 0.5, 1.0, 2.0, and 5.0 M NaCl, sequentially. Each subfraction was collected, desalted *via* ultrafiltration

using 3 kDa filters, and freeze-dried.

2.3. Molecular weight determination

Molecular weight determination was performed using size exclusion chromatography with sequential TSKgel G6000PW and TSKgel G4000SWXL columns (Tosoh Bioscience, South San Francisco, CA). The mobile phase consisted of aqueous 0.1 M sodium sulfate, and the flow rate was set at 0.5 mL/min. For each run, 100 μg of each sample was dissolved in the mobile phase and injected into a Shimadzu LC-10 A HPLC (Carlsbad, CA) equipped with a refractive index detector. A calibration curve was established using a cubic fit and polysaccharide standards including *iota*-carrageenan (M_w = 2400 kDa) (FMC, Philadelphia, PA) and a series of dextran standards (M_w = 1–670 kDa) (Millipore Sigma) to determine molecular weight.

2.4. Sulfate content determination

Glycan sulfate content was determined using the $BaCl_2$-gelatin turbidimetric method. Briefly, 1–5 mg samples were hydrolyzed with 1 mL of 2 M hydrochloric acid at 70 °C overnight. Then, 80 μL of the hydrolysate was mixed with an equal volume of 1 % gelatin (*w/v*) and 20 % $BaCl_2$ (w/v) in a 96-well plate. A calibration curve was established using aq. K_2SO_4 solution with concentrations ranging from 0 to 0.05 % (w/v). Samples were then analyzed spectrophotometrically at 600 nm in a plate reader (BioTek Synergy 4, Agilent, Santa Clara, CA).

2.5. Monosaccharide analysis

Glycan samples were labeled with 1-phenyl-3-methyl-5-pyrazolone (PMP) and analyzed using HPLC-MS in multiple reaction monitoring (MRM) mode following the method of Xu (Xu et al., 2018) with modifications. Glycan samples were dissolved in water to prepare a 1 mg/mL solution, and an equal volume of 4 M hydrochloric acid was added. Hydrolysis was conducted at 85 °C for 8 h, followed by overnight incubation at RT. The pH was adjusted to neutral using 4 M aq. NaOH. Subsequently, 200 μL of hydrolysate were mixed with an equal volume of 0.25 M PMP, which had been prepared using a 0.4 M aq. ammonium hydroxide solution containing 25 % (*v*/v) methanol. This mixture was incubated at 70 °C for 90 min, and then cooled to RT. The pH was adjusted to neutral using a 0.8 M aq. formic acid solution. To remove residual PMP, chloroform was added, and the lower layer was discarded. This extraction process was repeated 2–3 times. Monosaccharide reference standards including mannose, glucosamine, rhamnose, glucose, galactose, fucose, xylose, arabinose and glucuronic acid, underwent the same pre-column derivatization procedure. HPLC was performed using an Agilent 1200 LC system with an Agilent Poroshell 120 EC-C18 column (2.7 μm, 2.1 × 100 mm) at 35 °C. *mobile* phase A consisted of 25 mM aq. ammonium acetate containing 5 % (v/v) acetonitrile adjusted to pH 8.2 using ammonium hydroxide. Mobile phase B consisted of 95 % (v/v) acetonitrile in water. The mobile phases were delivered through the column at a flow rate of 200 μL/min. The gradient elution profile was as follows: 0.0–9.0 min, 14–20 % B; 9.01–9.5 min, 20–95 % B; 9.51–12.5 min, 95 % B; 12.51–19.5 min, 14 % B. Prior to injection into the HPLC, the derivatized samples were diluted 20-fold with mobile phase A, and a volume of 5 μL was injected. A triple quadrupole MS system equipped with an electrospray ionization source (ThermoFisher Scientific, Waltham, MA) was used as the detector. MS analysis was performed in positive ionization mode with a spray voltage of 2500 V, a vaporizer temperature of 300 °C, and a capillary temperature of 350 °C. The online MS analysis was conducted in the multiple reaction monitoring mode.

2.6. Structural characterization of FSjRPI-27 using nuclear magnetic resonance (NMR) spectroscopy

One F*Sj*RPI-27 subfraction, F*Sj*RPI-$27_{>100kDa\ (5M)}$, and two subfractions of F*Sj*RPI-28 (oxidatively degraded F*Sj*RPI-27), F*Sj*RPI-$28_{3\text{-}10kDa\ (1M)}$ and F*Sj*RPI$28_{3\text{-}10kDa\ (2M)}$, were selected for NMR analysis. For the 1D ^1H and 2D NMR, 10–15 mg of the samples were dissolved in D_2O and freeze-dried. The procedure was repeated three times. The samples were finally dissolved in D_2O at 20 mg/mL. The 1D ^1H NMR and 2D NMR including ^1H—^{13}C HSQC, ^1H—^1H TOCSY, and ^1H—^1H NOESY were recorded on a Bruker 800 MHz spectrometer (Billerica, MA, USA) at 298 K. For the 1D ^{13}C NMR, 10–15 mg of the samples were dissolved in 500 μL of D_2O. added with 5 μL of 50 mM sodium trimethylsilylpropanesulfonate. The data was recorded at 343 K for 23 h. The spectra were processed using Topspin 3.6.5 software, peaks were assigned according to published data (Bilan et al., 2004, 2006; Clément et al., 2010; Heiss et al., 2021).

2.7. Permethylation and glycosyl linkage analysis

Permethylation analysis was conducted using F*Sj*RPI-$28_{3\text{-}10kDa\ (1M)}$ and F*Sj*RPI-$28_{3\text{-}10kDa\ (2M)}$ in both original and desulfated forms. For the original form, 1.5 mg of each glycan was passed through Dowex 50 cation exchange resin and converted to the triethylammonium form before the linkage analysis. For the desulfated form, 2.0 mg of each glycan were passed through Dowex 50 cation exchange resin and converted to the pyridinium form. Additionally, freeze-dried samples were desulfated by incubating them in a mixture of 89:10:1 DMSO:MeOH: pyridine (v:v:v) for 4 h at 100 °C, followed by dialysis to remove DMSO. Samples were then freeze-dried before the linkage analysis. Dried original and desulfated samples were dissolved in 300 μL of DMSO, left to stir for 24 h, and then subjected to three rounds of treatment with sodium hydroxide and methyl iodide. Excess iodomethane was removed by purging samples with N_2, and permethylated derivatives were recovered from the reaction by passing through the C18 Sep-Pak reverse-phase cartridge. The permethylated samples were hydrolyzed using 2 M TFA for 2 h at 121 °C, reduced with $NaBD_4$, and converted to alditol acetates with acetic anhydride in the presence of pyridine. The derivatives were analyzed using an Agilent 7890 A GC interfaced to a 5975C MSD (mass selective detector, electron impact ionization mode). Separation was performed on a 30 m Supelco SP-2331 bonded phase fused silica capillary column.

2.8. SPR solution competition assay

Solution competition assays between surface-bound heparin and glycans were conducted in buffer using a BIAcore T200 instrument and analyzed with T200 evaluation software (Uppsala, Sweden). Biotinylated heparin was prepared and immobilized onto a SA chip following the manufacturer's protocol. The WT SARS-CoV-2 SGP RBD, was mixed with various concentrations of glycans in HBS-P buffer (0.01 M 4-(2-hydroxyethyl)-1-piperazineethanesulfonic acid, 0.15 M NaCl, 0.005 % surfactant P20, pH 7.4). The mixtures were injected over the heparin chip at a flow rate of 30 μL/min for 180 s. After each run, dissociation and regeneration were performed by injecting 2 M NaCl for 100 s. To provide comparison to the algal polysaccharide, the same RBD solution mixed with heparin and PPS in the running buffer was also tested. Additionally, for quality control, a run with only the RBD protein was performed after every 10 competition experiments. This control run ensured that the chip surface was fully regenerated and that the results obtained among runs were comparable.

2.9. Generation of WT Pseudovirus and neutralization assay

Lenti-X™ 293 T cells (Takara Bio) were grown in Gibco™ Dulbecco's Modified Eagle Medium (DMEM) (Thermo Fisher Scientific)

supplemented with 10 % fetal bovine serum (FBS). These cells were transfected with plasmids psPAX2 (a gift from Didier Trono; Addgene plasmid #12260), pLV-eGFP (a gift from Pantelis Tsoulfas; Addgene plasmid #36083) and pCAGGS-S (expressing SARS-CoV-2 spike glycoprotein, Wuhan-Hu-1 strain) (BEI Resources). TransIT™-Lenti Transfection Reagent (Mirus Bio, Madison, WI) was used as the transfection reagent according to the manufacturer's protocol. The cell free media from the transfected cells were collected at 48 h and 72 h post transfection, and then pooled and centrifuged at 4000 rpm for 5 min to remove cell debris. The resulting suspensions were then passed through a 0.45 μm filter and subjected to sucrose cushion centrifugation at 10,000 ×*g* for 4 h. The pseudovirus pellet was washed from the tubes using Gibco™ Dulbecco's phosphate-buffered saline (DPBS) (ThermoFisher Scientific) and Lenti-X™ Concentrator (Takara Bio, San Jose, CA) was added to the DPBS. It was then processed according to the manufacturer's protocol to prepare concentrated pseudovirus.

For neutralization studies, a 96-well plate was coated with 1 % fibronectin and seeded with human ACE2 HEK-293 T cells (Takara Bio), 20,000 cells/well. After overnight incubation at 37 °C with 5 % CO_2 in DMEM supplemented with 10 % FBS, spike wild-type (WT) pseudovirus, prepared from the 2-step concentration protocol described above, was used at a titer of 2.0×10^6 TU/mL. Glycans were dissolved in DPBS to provide stock solutions of 2 mg/mL and were filter sterilized with 0.22 μm polyvinylidene difluoride membrane filters. The glycans were diluted in DMEM at concentrations ranging from 6.4 ng/mL to 1 mg/mL, WT pseudovirus was added, and the suspensions were incubated for 1 h at 37 °C followed by adding to the cells in the 96-well plates. The cells were incubated with the pseudovirus particles and glycans for 2 h at 37 °C followed by media exchange to DMEM supplemented with 10 % FBS. At 48 h post-infection, the cells were stained with Hoechst 3342 for 10 min, cell media was changed to Gibco™ FluoroBrite™ DMEM (ThermoFisher Scientific), and the plate was imaged using the Thermo Scientific™ Cellomics ArrayScan™ XTI. Images were analyzed using the Target Activation Bioapplication feature. Three technical replicates were performed for each glycan concentration.

2.10. SARS-CoV-2 virus preparation

SARS-CoV-2 virus (Coronavirus strain 2019-nCoV/USA-WA1/2020, no. NR-52281) was obtained from BEI Resources, NIAID, NIH. Preparation of SARS CoV-2 virus stock was performed as described by Singh et al. (2021). Briefly, exponentially dividing Vero E6 cells were infected at ≥80 % confluency with SARS CoV-2 virus at a multiplicity of infection of 0.01. The cells were then incubated at 37 °C in 5 % CO_2 for 3–4 days or until ≥50 % cytopathic effects were observed. Virus was purified from cell-free culture supernatants using an Abcam PEG purification kit (ab102538). The purified virus was resuspended in sterile phosphate buffered saline (PBS) and frozen at −80 °C until use.

2.11. Mouse infections

All animal experiments adhered to the ARRIVE guidelines 2.0. Male and female hACE2 receptor–transgenic mice (K18-hACE2 mice) were purchased from The Jackson Laboratory, bred in the Albany Medical College Animal Resource Facility, and used at 6–8 weeks of age. Due to the heterozygous expression of the *hACE-2* gene in these animals, all mice used in the study were polymerase chain reaction verified for the presence of the hACE-2 receptor. For infection, mice were anesthetized *i.p.* with 20 % ketamine (100 mg/mL) and 5 % xylazine (20 mg/mL) in PBS and inoculated *i.n.* with 40 μL of SARS CoV-2 (1×10^4 or 5×10^4 plaque-forming units (PFU) per mouse) that was diluted in sterile PBS. For the fucoidan treatment, equal numbers of randomly selected male and female mice were anesthetized with 3 % isoflurane and inoculated *i.n.* with F*Sj*RPI-27or F*Sj*RPI-28 (100 μg in 40 μL of PBS) 6 h before infection, simultaneously with infection and every 48 h until 6 days post-infection (dpi). Control mice were infected and inoculated with equal volumes of sterile PBS at the same timepoints. Infected animals were housed in individually ventilated cages within the Albany Medical College ABSL-3 facility. Mortality and body weight changes were monitored daily until dpi 15. For survival, weight change, and viral titer measurements, no animals were excluded from the analyses.

2.12. Pulmonary SARS-CoV-2 virus titers

SARS CoV-2 titers in lung homogenates and bronchoalveolar lavages (BAL) were determined as described previously by Singh et al. (2021). In brief, Vero E6 cell monolayers were infected with serially diluted cell-free lung homogenates and BAL samples for 1 h at 37 °C with gentle rocking every 15 min. The infected cell monolayers were then incubated in DMEM containing 2 % FBS, 1 × PSN (Penicillin-Streptomycin-Neomycin), and 1 % methylcellulose. On day 4 post infection, the cells were fixed with 10 % formalin for 1 h followed by staining with 1.0 % crystal violet. Plaques were counted manually under 10× magnification.

2.13. Ethical statement

All animal protocols in this study were approved by the Albany Medical College AMC Animal Care and Use Committee (IACUC) protocol #22–12,003 and follow the ARRIVE guidelines 2.0.

2.14. Statistical analyses

Spearman's correlation was conducted using R to analyze the IC_{50} values from the SPR assay and selected compositional features of various glycans, including fractionated algal glycans, heparin, and PPS. The compositional features include log of molecular weight, sulfate content, and ratios of galactose, fucose, and methyl pentose, respectively. Statistical analysis of mouse survival was performed by the log-rank Mantel Cox test. Daily monitoring of the mouse groups (8 mice/group, randomly assigned) provided 80 % power to detect a 4-day difference in survival compared to control animals. Lung and BAL viral titers were analyzed by two-way ANOVA with Tukey's multiple comparisons.

3. Results

3.1. Physicochemical properties of algal glycan subfractions

3.1.1. Fractionation

The overall weight recovery of F*Sj*RPI-27, F*Sj*RPI-28, and algal crude extracts after MWCO fractionation was 74–88 %. The resulting major fractions were further subjected to strong-anion-exchange (SAX) fractionation, with a further weight recovery of 68–95 %. F*Sj*RPI-27 consists predominantly of high-molecular-weight polysaccharides, with M_n = 147 kDa and polydispersity index (PDI, M_w/M_n) = 1.19 (Table 1). Following MWCO fractionation the >100 kDa fraction was nearly 5-fold in excess of the 30–100 kDa fraction (Fig. 1A-i). Relatively high salt was required to elute the two major F*Sj*RPI-27 fractions from the SAX column; the higher molecular weight fraction requiring 5 M aq. NaCl for greater elution than the lower molecular weight fraction (Fig. 1A-ii, Fig. S2B, Table 1). Four major subfractions were obtained from SAX separation and used in further studies: F*Sj*RPI-$27_{>100kDa\ (2M)}$; F*Sj*RPI-$27_{>100kDa\ (5M)}$; F*Sj*RPI-$27_{30\text{-}100kDa\ (2M)}$; and F*Sj*RPI-$27_{30\text{-}100kDa\ (5M)}$. F*Sj*RPI-28 yielded three major MWCO fractions (Fig. 1B-i): 30–100 kDa, 10–30 kDa, and 3–10 kDa, with over half <30 kDa, and with very little elution beyond 2 M aq. NaCl (Fig. 1B-ii). Six subfractions were isolated and used in further assays: F*Sj*RPI-$28_{30\text{-}100kDa\ (1M)}$; F*Sj*RPI-$28_{30\text{-}100kDa\ (2M)}$; F*Sj*RPI-$28_{10\text{-}30kDa\ (1M)}$; F*Sj*RPI-$28_{10\text{-}30kDa\ (2M)}$; F*Sj*RPI-$28_{3\text{-}10kDa\ (1M)}$; and F*Sj*RPI-$28_{3\text{-}10kDa\ (2M)}$ (Table 1).

M_w and M_n of the F*Sj*RPI-28 series were not provided, because the major glycan peak could not be separated from the salt peak (Fig. S2C), which prevented accurate M_w and M_n calculations. Therefore, only the peak molecular weight (M_p) is provided for the F*Sj*RPI-28 series. The

Table 1
The molecular weight, compositional information and IC_{50} value of inhibiting S-protein RBD binding to heparin chip of different glycan fractions.

Glycan fractions		Molecular weight (kDa) [a]			Sulfate content (%, *w*/w)	Ave sulfate number per mono-saccharide	Monosaccharide composition (molar %)									IC_{50} of inhibiting SGP RBD binding to heparin chip (ng/mL) [b]
		Mw	Mn	Mp			Man	GlcN	GlcA	Rha	Glc	Gal	Xyl	Ara	Fuc	
FS*j*RPI-27	unfractionated	174.2	146.8	352.3	27.9 ± 0.5	0.58	1.5	N.D.	0.8	0.9	0.6	36.3	1.5	0.2	58.3	65.6
	>100 kDa (2 M)	167.7	143.9	–	33.2 ± 3.2	0.74	2.2	N.D.	2.7	0.8	0.4	42.8	0.6	N. D.	50.5	60.0
	>100 kDa (5 M)	264.1	230.7	450.4	33.8 ± 0.5	0.76	0.9	N.D.	0.7	0.5	0.2	51.8	0.4	0.5	45.0	43.4
	30-100 kDa (2 M)	54.4	44.8	27.1	31.5 ± 1.0	0.68	1.6	N.D.	2.3	0.5	4.0	33.8	0.6	0.2	56.9	100.1
	30-100 kDa (5 M)	131.2	112.2	126.4	31.8 ± 1.2	0.69	0.3	N.D.	0.2	0.1	0.4	45.4	0.2	0.3	53.1	61.9
FS*j*RPI-28	unfractionated	–	–	5.4	26.5 ± 0.7	0.54	3.8	N.D.	2.2	2.7	6.6	24.5	4.9	N. D.	55.3	1097
	30-100 kDa (1 M)	–	–	7.6	18.4 ± 1.0	0.35	13.4	N.D.	11.6	2.4	3.3	22.1	5.7	N. D.	41.5	7073
	30-100 kDa (2 M)	–	–	10.0	36.4 ± 0.9	0.82	4.3	N.D.	3.2	0.9	1.0	20.0	1.1	N. D.	69.5	341.3
	10-30 kDa (1 M)	–	–	5.1	27.0 ± 0.3	0.56	8.5	N.D.	7.6	1.5	1.8	28.2	2.7	0.3	49.3	~ 625,000 [b]
	10-30 kDa (2 M)	–	–	6.5	38.0 ± 0.7	0.87	2.7	N.D.	2.3	0.4	0.4	17.6	0.6	0.2	75.8	1037
	3-10 kDa (1 M)	–	–	3.6	25.3 ± 1.0	0.52	5.3	N.D.	9.4	1.3	1.2	33.4	1.2	0.3	48.0	> 625,000 [b]
	3-10 kDa (2 M)	–	–	4.3	37.1 ± 1.2	0.84	2.3	N.D.	2.7	0.3	0.6	21.4	0.2	N. D.	72.5	15,000
FS*l*	Crude extract	46.4	33.7	16.0	8.5 ± 0.5	0.15	2.1	0.6	1.4	3.4	64.2	11.5	4.1	0.5	12.2	5698
	>100 kDa (1 M)	282.6	231.7	551.8	6.2 ± 0.3	0.10	10.1	2.9	17.2	6.8	7.4	8.7	12.8	N. D.	34.1	10,009
	>100 kDa (2 M)	262.3	235.6	343.1	20.9 ± 0.7	0.41	6.8	1.8	7.6	6.8	3.6	45.3	3.2	0.2	24.7	1849
RS*Mn*	Crude extract	369.9	313.0	122.8	24.8 ± 0.8	0.48	2.2	0.0	3.8	68.7	9.1	2.3	8.3	1.7	4.0	53.9
	>100 kDa (2 M)	198.7	169.7	–	27.9 ± 0.4	0.56	2.0	0.0	4.4	68.0	8.8	4.1	8.3	1.2	3.2	71.3
	>100 kDa (5 M)	389.3	338.4	119.0	32.4 ± 0.4	0.68	1.3	0.0	3.6	73.0	5.9	3.4	8.1	0.9	3.8	49.1

N.D.: Not detected.

[a] The weight-average molecular weight (Mw), number-average molecular weight (Mn), and peak molecular weight (Mp) of the algal glycan fractions are provided. "-": For the FS*j*RPI-27$_{>100kDa\ (2M)}$ and RS*Mn*$_{>100kDa\ (2M)}$, Mp was not provided due to the lack of a distinctive major peak (Fig. S2). For the FS*j*RPI-28 series and PPS, only Mp was provided, as the major glycan peak is not separated from the salt peak, which would compromise the Mw and Mn calculations.

[b] The binding of RBD-surface heparin was 44.3 % and 88.9 % of the control in the presence of 625 μg/mL FS*j*RPI-28$_{10\text{-}30kDa\ (1M)}$ and FS*j*RPI-28$_{3\text{-}10kDa\ (1M)}$, respectively.

crude polysaccharide extract from *S. latissima* was a fucoidan (FS*l*) with a relatively high proportion of small polysaccharide chains of M_n 33.7 kDa (Table 1 and Fig. S2D). These MWCO fractions were somewhat intermediate to those of FS*j*RPI-27 and FS*j*RPI-28, made up of roughly evenly split fractions of >100 kDa, 30–100 kDa, and < 30 kDa (Fig. 1C-i). Based on SAX analysis (Fig. 1C-ii), the 30–100 kDa fraction contained approximately 60 % of the component unbound to the SAX column, likely indicating the presence of laminarin in the crude extract, which is known to be present in brown seaweed kelp (Sterner & Gröndahl, 2021). The subfractions selected for further investigation from FS*l*, these were FS*l*$_{>100kDa\ (1M)}$ and FS*l*$_{>100kDa(2M)}$. These subfractions of FS*l* had quite high molecular weights (Table 1, Fig. S2D) resulting from the removal of a large fraction of the low molecular weight chains that had been present in the crude FS*l* extract.

Finally, the crude extract from *M. nitidum* (RS*Mn*) was predominantly composed of very high molecular weight components (M_n = 313 kDa; Table 1 and Fig. S2E) and required a high-salinity NaCl solution for elution from the SAX column, which suggested it was riched in rhamnan sulfate. Consequently, two subfractions were isolated and used in further assays: RS*Mn*$_{>100kDa\ (2M)}$ and RS*Mn*$_{>100kDa\ (5M)}$.

3.1.2. Compositional analysis

FS*j*RPI-27 and its subfractions had relatively high sulfate content (28–34 %, *w*/w), with approximately 95 % (*w*/w) fucose and galactose (Table 1, Fig. S3). Among the FS*j*RPI-27 subfractions, FS*j*RPI-27$_{>100kDa\ (5M)}$ exhibited the highest galactose and lowest fucose contents. The lower sulfate content in the unfractionated FS*j*RPI-27 was due to the presence of impurities including alginate, indicated by the presence of mannuronic acid (Fig. S3B, asterisk) derived from alginate's partial hydrolysis. These components were removed by SAX fractionation. Interestingly, there was essentially no difference in sulfate content between 2 M and 5 M SAX elution fractions. In contrast, FS*j*RPI-28 subfractions eluted with 2 M NaCl displayed higher sulfate content compared to their 1 M counterparts. In addition, compared to FS*j*RPI-27 and its subfractions, the FS*j*RPI-28 series is generally lower in galactose content. The crude extract and MWCO/SAX fractions from *S. latissima* (Table 1) contained a much lower sulfate content than FS*j*RPI-27 and FS*j*RPI-28. Moreover, the crude extract contained a significant amount of glucose, likely derived from laminarin. The monosaccharide composition of the subfractions from *S. latissima* was complex, with a higher abundance of mannose, galactose, xylose, glucuronic acid, and a small amount of glucosamine. The crude extract and subfractions from the *M. nitidum* were predominantly rhamnose (RS*Mn*) (approximately 70 mol%),

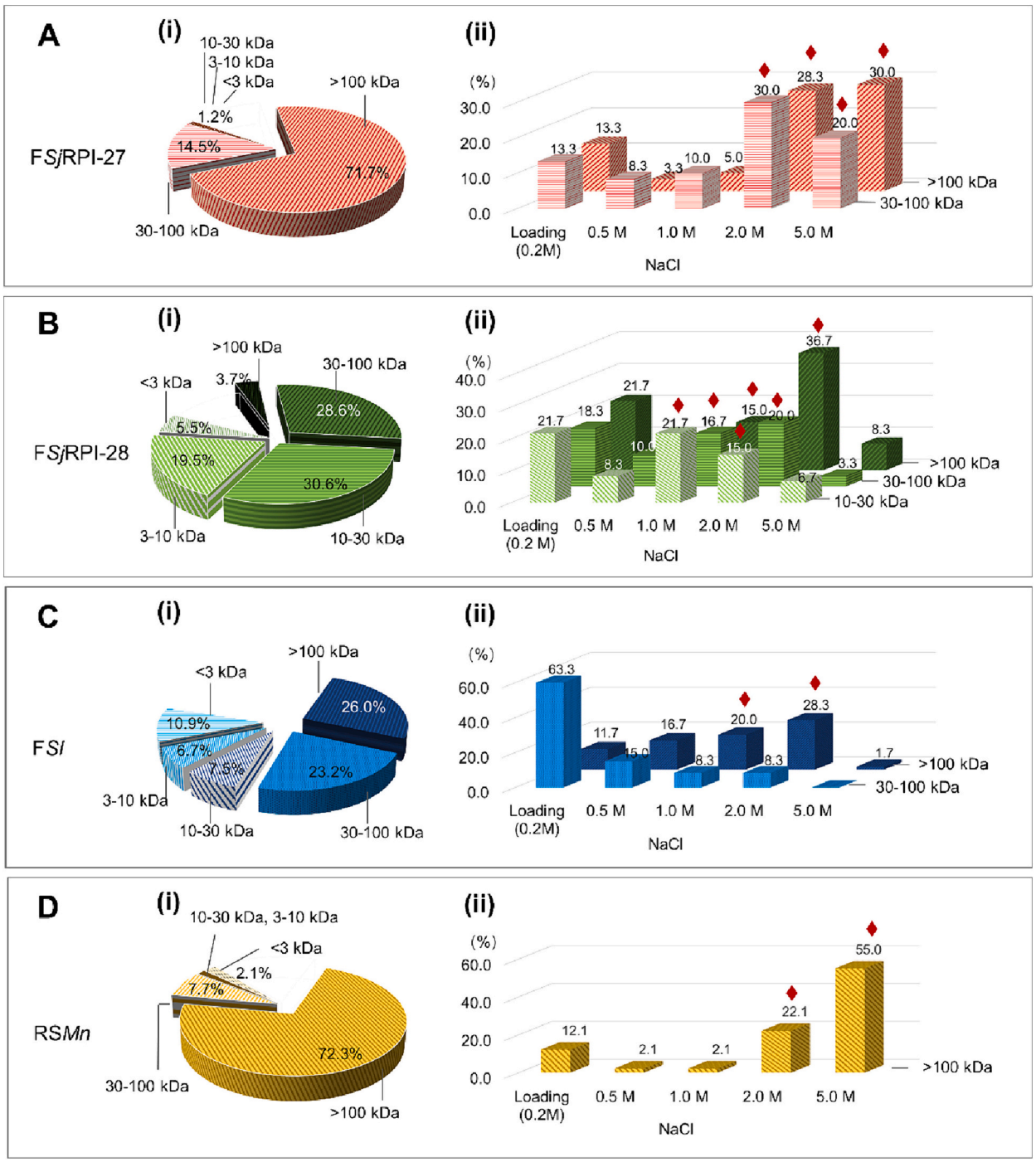

Fig. 1. The recovery of algal glycan samples from molecular weight cut-off (MWCO) and strong anion exchange (SAX) for each algal sample. FS*j*RPI-27, FS*j*RPI-28, crude extract from *S. latissima* (FS*l*) and *M. nitidum* (RS*Mn*) are depicted in A, B, C, D, respectively. The pie charts (i) illustrate the recovery after MWCO fractionation, and the bar graphs (ii) show the recovery from SAX separation of the major fractions following MWCO fractionation. The diamond indicated subfractions were selected for SPR assay.

followed by glucose and xylose, with an increased sulfate content in SAX elutions at higher NaCl concentration. The average sulfate number per monosaccharide for algal polysaccharide subfractions range from 0.10 to 0.87 (Table 1).

3.2. Structural characterization of FSjRPI-27 and FSjRPI-28

The three subfractions, FS*j*RPI-27$_{>100kDa\ (5M)}$, FS*j*RPI-28$_{3\text{-}10kDa\ (1M)}$, and FS*j*RPI-28$_{3\text{-}10kDa\ (2M)}$ were selected as representative fucoidan extracts to elucidate the structure of FS*j*RPI-27, due to their differences in molecular weight and monosaccharide compositions. The ^{1}H spectrum of FS*j*RPI-27$_{>100kDa\ (5M)}$ revealed that the polysaccharide is heavily acetylated, evident from an overlapping peak around 2.1 ppm (Fig. S4A). However, both FS*j*RPI-28 subfractions showed negligible acetylation (Fig. S4B, C), suggesting that the acetylated saccharide units were susceptible to H_2O_2 degradation. The fucoidan molecules are high in molecular weight, which results in very broad carbon signals due to shorter T2 relaxation. For this reason, 1D ^{13}C NMR was recorded at 343 K for 23 h to obtain appropriate spectra for assignment (Fig. S5). Similar to the ^{1}H spectra, the ^{13}C spectra also confirmed that the acetylated

saccharide units in the two FS*j*RPI-28 subfractions were essentially undetectable. The 2D NMR spectra of FS*j*RPI-27$_{>100kDa\ (5M)}$, FS*j*RPI-28$_{3\text{-}10kDa\ (1M)}$, and FS*j*RPI-28$_{3\text{-}10kDa\ (2M)}$ are provided in Figs. S6-S8, respectively. The detailed ^{1}H and ^{13}C NMR chemical shift assignments of the intense signal (major residues) are provided in Table S1. The HSQC spectra revealed that the galactose unit is highly structurally diverse and responsible for the high degree of fucoidan acetylation. The glycosidic linkage for the galactose occurs at C2/C3/C6, the acetylation occurs at C2/C3/C4, and the galactose units can be sulfated at the C3 hydroxyl groups. A variety of galactose units with different degrees of acetylation and sulfation exist, including but not limited to, a triacetylated component →6)β-Gal-2,3,4-tri-*O*-acetyl-(1→, diacetylated unit →6)β-Gal-2,3-di-*O*-acetyl-(1→, and sulfated unit →6)β-Gal-3-SO_3^--(1→. The fucose units were only observable in the anomeric region of the HSQC spectrum of FS*j*RPI-27$_{>100kDa\ (5M)}$. However, the fucose signals were significantly enhanced in the spectra of the FS*j*RPI-28 subfractions, which were deacetylated during degradative processing with H_2O_2. A major fucopyranose structure is →3)α-Fuc-4-SO_3^--(1→. In the HSQC spectrum of FS*j*RPI-28$_{3\text{-}10kDa\ (2M)}$, which is a relatively low molecular weight, but highly sulfated, subfraction, the signal intensity of disulfated residue →3)α-Fuc-2,4-SO_3^--(1→, was significantly increased. The →6)β-Gal-3-SO_3^--(1 → has a relatively high signal intensity, especially in the fucose-enriched degraded subfractions, suggesting that it is a major component of the polysaccharide backbone, especially the part close to non-reducing termini.

Permethylation linkage analysis consistently aligned with the findings from 2D NMR analysis. Given the high acetylation of FS*j*RPI-27$_{>100kDa\ (5M)}$, we specifically targeted two subfractions from FS*j*RPI-28 for linkage analysis to mitigate potential confounding effects of acetyl groups. The results of permethylation analysis were corroborated with the monosaccharide composition of the two target subfractions, and the relative percentages of Fuc*p* and Gal*p* residues before and after desulfation are provided in Table S2. Both subfractions exhibited an elevation in the percentage of terminal groups (t-Fuc*p* and t-Gal*p*) after desulfation, suggesting the presence of sulfated terminal groups. Concurrently, the proportion of 3,6-Gal*p* decreased while that of 6-Gal*p* increased, consistent with the predominant residue →6)β-Gal-3-SO_3^--(1 → detected by 2D NMR. Moreover, both subfractions exhibited a reduction in 3,4-Fuc*p* and 2,3,4-Fuc*p* residues, alongside an increase in 3-Fuc*p*, mirroring the major fractions →3)α-Fuc-4-SO_3^--(1 → and →3)α-Fuc-2,4-SO_3^--(1 → identified by 2D NMR. However, a decrease in the percentage of 2-Fuc*p* post-desulfation indicated the presence of terminal 2-Fuc*p*, not discernible from 2D NMR spectra. Additionally, the FS*j*RPI-28$_{3\text{-}10kDa\ (1M)}$ displayed a notable rise in 3-Gal*p* post-desulfation, suggesting the presence of sulfated 3-Gal*p* residues not identified by either 2D NMR or permethylation analysis.

3.3. *In vitro biological activity analysis of algal fractions*

3.3.1. *SPR solution competition*

SGP is known to bind to heparin that is coated on an SPR sensor chip (Kim et al., 2020). Competitive inhibition of this binding represents a quantitative, albeit indirect, assessment of the potency of blocking the interaction of SGP with target cell HS. To this end, we examined the effect of various algal subfractions on inhibiting SGP RBD-heparin interaction. Dose response curves for each algal subfraction, along with crude or unfractionated materials, are shown in Fig. 2 and calculated IC_{50} values are listed in Table 1. Dose response curves for heparin

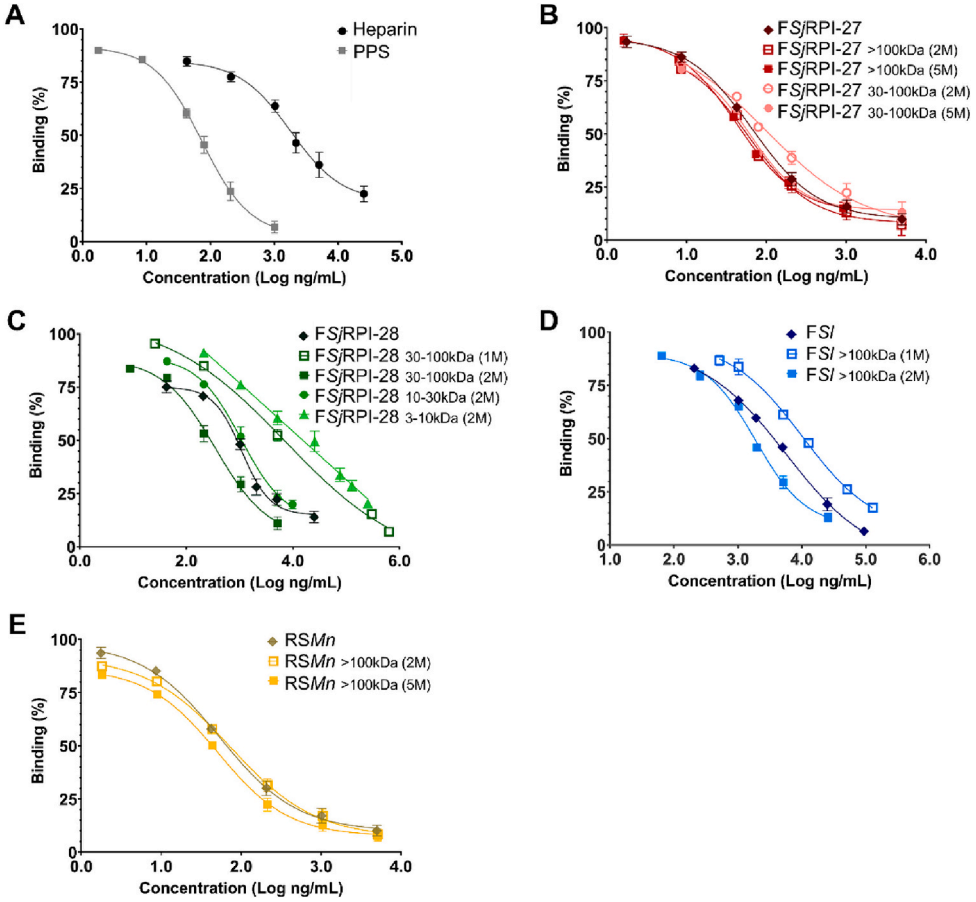

Fig. 2. Dose response curves of inhibitory activities of fucoidan fractions, heparin and PPS on WT SARS-CoV-2 SGP RBD-heparin SPR chip binding. A, heparin and PPS; B, unfractionated FS*j*RPI-27 and the subfractions; C, unfractionated FS*j*RPI-28 and subfractions; D, crude extract of *S. latissimi* (FS*l*); E. rhamnan sulfate crude extract (RS*Mn*) and the subfractions. The FS*j*RPI-28 $_{3\text{-}10kDa\ (2M)}$ was fit with linear model, the rest were fit with logistic curve.

and PPS are shown for comparison in Fig. 2A, giving rise to IC_{50} values of 1.8 μg/mL and 74 ng/mL, respectively, and are consistent with previous studies (Kim et al., 2020; Shi et al., 2022).

The FS*j*RPI-27 series (Fig. 2B) exhibited significant competitive inhibition activity against SGP binding to heparin, with an $IC_{50} = 43.4$ ng/mL for the >100 kDa, 5 M NaCl subfraction, which was slightly more inhibitory than that for the >100 kDa, 5 M NaCl subfraction from rhamnan sulfate (RS*Mn*). The FS*j*RPI-28 series (Fig. 2C) and subfractions from *S. latissima* (Fig. 2D) were less potent inhibitors than FS*j*RPI-27 and rhamnan sulfate (RS*Mn*) (Fig. 2E), although some of these subfractions were still potent in blocking SGP RBD-heparin binding, *e.g.*, FS*j*RPI-$28_{30\text{-}100kDa\ (2M)}$ with $IC_{50} = 341$ ng/mL.

3.3.2. Inhibition of WT pseudovirus cell entry using sulfated glycans

Inhibition of cell-based infection provides a more granular assessment of the potency of the sulfated polysaccharides. Thus, we examined the effect of a subset of the glycan extracts, including unfractionated FS*j*RPI-27 and FS*j*RPI-28, and rhamnan sulfate (RS*Mn*). Pseudovirus particles containing surface Wuhan-Hu-1 SGP were prepared and infection of human ACE2 HEK-293 T cells was assessed in 96-well plates. Inhibition of entry was evident *via* decreased fluorescence in each well (representative wells for each glycan tested) as a function of glycan concentration (Fig. 3A). From the dose response curves (Fig. 3B), IC_{50} values of unfractionated FS*j*RPI-27 and RS*Mn* were 0.52 and 0.93 μg/mL respectively. These fractions were significantly more potent than PPS and heparin, which had IC_{50} values of 1.6 and 4.6 μg/mL, respectively. Interestingly, unfractionated FS*j*RPI-28 did not generate a dose response curve due to its more limited capacity to inhibit cell entry of pseudovirus, which is consistent with its relatively low inhibitory activity against SGP-heparin binding (see above).

3.4. In vivo FSjRPI-27 and FSjRPI-28 anti-SARS-CoV-2 activity

The effectiveness of fucoidans in competitive binding and cell-based studies suggested that they could be useful as a prophylactic glycan against SARS-CoV-2 infection. Consistent with the *in vitro* study, *i.n.* treatment with FS*j*RPI-27 before and during an LD_{50} SARS-CoV-2 infection of hACE2 transgenic mice led to significant protection, with 100 % survival and no noticeable morbidity, as shown by the absence of weight loss (Fig. 4A-C). Treatment with FS*j*RPI-27 alone in the absence of infection likewise led to no changes in weight, indicating a lack of fucoidan toxicity. In contrast, FS*j*RPI-28-treated mice showed levels of mortality and weight changes similar to PBS-treated infected mice. We conclude that FS*j*RPI-27, but not FS*j*RPI-28, can mediate significant *in vivo* protection against SARS-CoV-2 infection.

The protective efficacy of FS*j*RPI-27 was further evaluated using a five-fold greater SARS CoV-2 infection dose. In this case, 85 % of PBS-treated mice succumbed to infection with substantial weigh loss (20–35 %) following challenge with SARS CoV-2 virus (Fig. 5A, B). In contrast, approximately two-thirds of the FS*j*RPI-27 treated mice survived and regained their body weight starting on day 7 post-infection. At 15 dpi, none of the surviving mice showed any apparent signs of disease.

We next measured viral loads in BAL and lung homogenates from animals infected with the higher dose of SARS-CoV-2 to determine whether FS*j*RPI-27 would prevent infection and/or enhance viral clearance. Compared to day 0, PBS-treated infected mice demonstrated a 2–3 $\log_{10}$ increase in BAL and lung viral titers at all timepoints (Fig. 6A-B). Conversely, on day 2 post challenge, BAL of RPI-27 treated mice had a moderate (1.5 $\log_{10}$) reduction in viral titers compared to PBS-treated infected mice (Fig. 6A). At 4 dpi, the BAL viral titers were further reduced to 2.67 $\log_{10}$ after RPI-27 treatment, and by 6 dpi, only one FS*j*RPI-27-treated mouse still contained detectable virus. Lung homogenates showed a 1 and 2 $\log_{10}$ reduction in viral burden at 2 and 4 dpi, respectively, after FS*j*RPI-27 treatment compared to PBS treatment (Fig. 6B). By 6 dpi, the mean lung homogenate viral titers in the FS*j*RPI-27 treated group was 2.13 $\log_{10}$ with no replicating virus detected in >33 % of the surviving mice. Taken together, the results indicate that FS*j*RPI-27 treatment reduces initial viral burden and also enhances viral clearance during the course of infection.

4. Discussion

A coupled fractionation procedure was used on the *S. japonica* and *S. latissima* fucoidans and *M. nitidum* rhamnan sulfate, including a

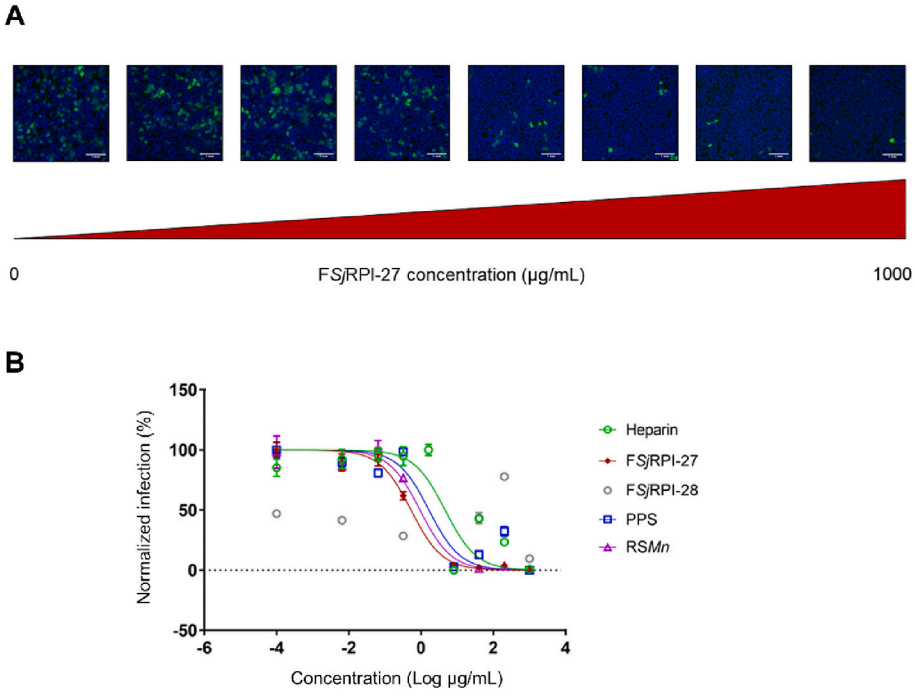

Fig. 3. A. Entry-level inhibition of WT by FS*j*RPI-27, shown by decreasing fluorescence with increasing concentration of the compound; B. Dose response curves against WT of various sulfated polysaccharides.

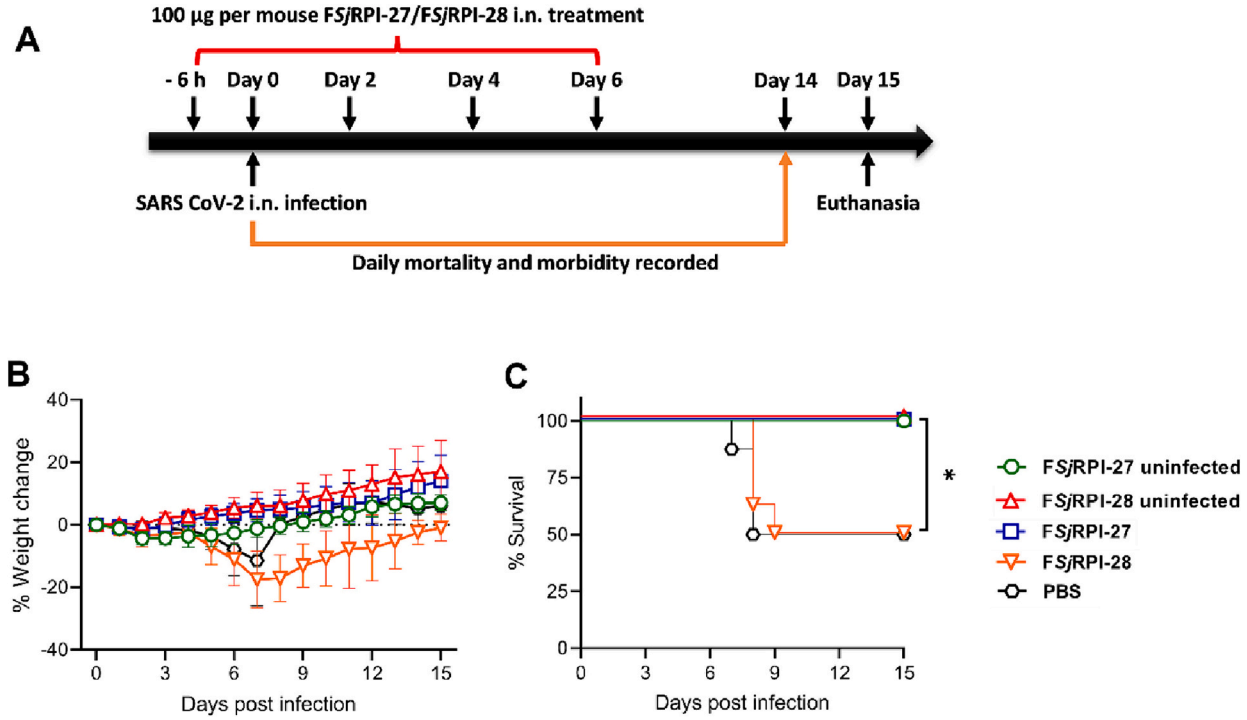

Fig. 4. Morbidity and mortality of mice after LD_{50} pneumonic infection with SARS-CoV-2 virus. A, Groups of mice were inoculated *i.n.* with 100 μg of F*Sj*RPI-27 or PBS at 6 h before infection, at the time of infection and at 2, 4 and 6 dpi. The mice were challenged *i.n.* with 1×10^4 PFU/mouse of SARS-CoV-2 purified virus on Day 0. Weight change (B) and survival (C) were monitored for 15 days post infection. Eight mice were used in each group. Survival was analyzed by Log rank Mantel-Cox test. *, $P < 0.05$.

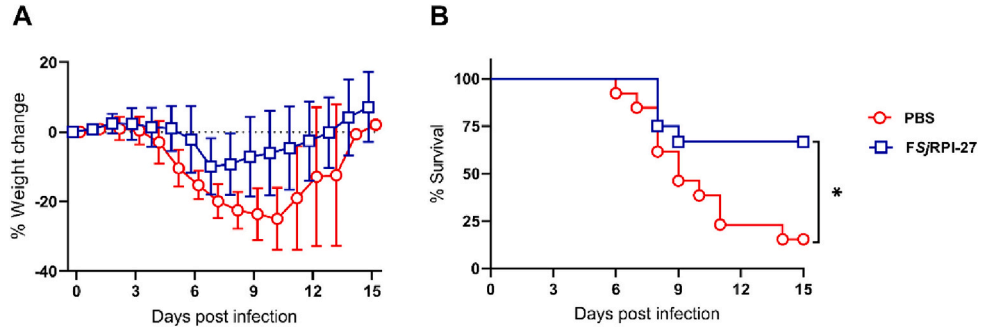

Fig. 5. Morbidity and mortality of mice after $5 \times LD_{50}$ pneumonic infection with SARS-CoV-2 virus. Groups of mice were inoculated *i.n.* with 100 μg of F*Sj*RPI-27 or PBS at 6 h before infection, at the time of infection and at 2, 4 and 6 dpi. The mice were challenged *i.n.* with 5×10^4 PFU/mouse of SARS-CoV-2 purified virus on Day 0. Weight change (A) and survival (B) were monitored for 15 days post-infection. Twelve mice (6 male and 6 female) in each group were used to assess mortality and morbidity. Survival was analyzed by Log rank Mantel-Cox test. *, $P < 0.05$.

MWCO and SAX step. The outcome of SAX separation appeared to correlate with the molecular weight of glycans. Overall, subfractions from the same glycan source material were within the same MWCO range, and as expected, the sulfate content increased as the eluent salinity increased. This pattern was observed for all algal polysaccharide subfractions except for F*Sj*RPI-27, wherein the sulfate levels were similar across the MWCO and SAX fractions. However, the molecular weights of F*Sj*RPI-27 were significantly distinct, with the higher molecular weight subfractions requiring higher salinity to be eluted. This indicates that the outcome of SAX separation depends on both the highly anionic sulfate residues and on glycan molecular weight. This result is reasonable considering that a larger negatively charged polysaccharide would have more sites to engage in binding to the SAX column, making it difficult to elute. Thus, a 2 M NaCl eluent may represent distinct sulfation levels, due to significant differences in molecular weight, such as $FSl_{>100kDa\ (2M)}$ and $FSjRPI\text{-}28_{3\text{-}10kDa\ (2M)}$. It is also worth noting that fucoidans in brown seaweeds vary not only among different species but also across different seasons, geographic locations, and even at different ages of the seaweeds (Bruhn et al., 2017). Consequently, the physicochemical characteristics of products obtained using the same purification protocol may not be identical if any of these factors change. Nevertheless, subfractions with higher molecular weight and sulfation levels can be recovered using a higher salinity of elution buffer in the SAX separation.

The activity of sulfated glycans has been linked to their molecular weight (Lahrsen et al., 2019; Ray et al., 2022; Sun, Ai, et al., 2023; Sun, Chopra, et al., 2023) and the degree of sulfation (Kopplin et al., 2018; Ray et al., 2022). Moreover, sulfation position and chain conformation can also impact polysaccharide antiviral bioactivity (Ray et al., 2022). To this end, we conducted a Spearman's correlation analysis of the SPR IC_{50} data and specific physicochemical features of the glycans (Fig. S9A), including all the algal subfractions, heparin, and PPS. Among

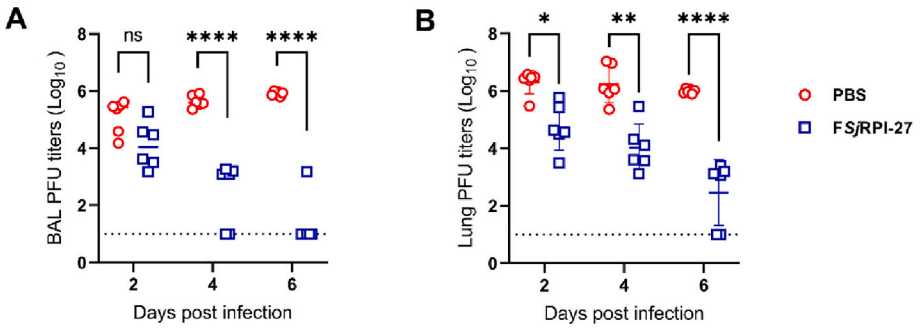

Fig. 6. Analysis of viral burden in mice after challenge with SARS-CoV-2 virus. Groups of mice were treated *i.n.* with 100 μg of F*Sj*RPI-27 or PBS at 6 h before infection, at the time of infection and at 2, 4 and 6 dpi. The mice were challenged *i.n.* with 5×10^4 PFU/mouse of SARS-CoV-2 purified virus on Day 0. Viral titers were measured in BAL (A) and lung homogenates (B) on 2, 4 and 6 dpi. Each group consisted of 6 mice (3 male and 3 female), indicated by individual symbols. Statistical variation between the groups was analyzed by two-way ANOVA and application of Tukey's test. The dotted line on each y-axis indicates the detection limit of 10 PFU. *, $P < 0.05$, **, $P < 0.01$; ****, $P < 0.0001$.

the selected physicochemical features, the log of molecular weight and sulfation level exhibited a moderate negative monotonic relationship with IC_{50}, with correlation values of −0.50 and − 0.40, respectively. Monosaccharide composition, including proportions of galactose, fucose, and methyl pentose (comprising both fucose and rhamnose), demonstrated a weak to very weak correlation with IC_{50}. Perhaps the most interesting correlation of IC_{50} was the product of molecular weight and sulfation content, with a correlation value of −0.89. This result suggests that log Mw multiplied by % sulfate content could be used to predict the glycan's RBD binding activity. Since the molecular weight and sulfate content were found to correspond strongly to the SGP RBD binding ability across structurally dissimilar polysaccharides, other factors, such as monosaccharide type and sulfation position, may not strongly influence virus binding. We further explored a potential quantitative model for RBD-sulfated glycan binding (Fig. S9B). A linear relationship exists between the reciprocal of IC_{50} and the (sulfate content) x $(\text{Log Mw})^{1.3–1.8}$, with a threshold to enter the linear range approximately at (sulfate content) x $(\text{Log Mw})^{1.5}$ of 2.5.

In our previous studies, we determined that sulfated polysaccharides are effective in inhibiting various SARS-CoV-2 variants using *in vitro* methods (Gelbach et al., 2022; Shi et al., 2022). However, in the current work, we selected the wild type for both *in vitro* and *in vivo* experiments. This decision was based on the consideration that wild-type SARS-CoV-2 has a lower positive surface charge in the spike RBD than in some of the variants (*i.e.*, Delta and Omicron), which have higher positive charges in the RBD (Kwon et al., 2023). This suggests that the inhibitory effect of sulfated polysaccharides would be less pronounced in the wild-type *vs.* the Delta and Omicron variants, and hence, would likely represent a minimal effective level of inhibitory activity.

Results obtained from our *in vitro* and *in vivo* studies confirmed that the higher molecular weight fucoidan, F*Sj*RPI-27, had a superior anti-SARS CoV-2 neutralizing property compared to the lower molecular weight F*Sj*RPI-28. This might be due to the higher molecular weight F*Sj*RPI-27 binding with greater avidity, *i.e.,* better multipoint binding, to the SGP of SARS-CoV-2 virus. Nevertheless, on 2 dpi after *in vivo* F*Sj*RPI-27 treatment, levels of SARS CoV-2 virus were lower but still detectable, both in extracellular (BAL) as well as intracellular (lung homogenates) samples. This is likely due to only partial blocking of virus attachment. Consistent with this, F*Sj*RPI-27 treated mice still lost significant weight early after infection (at the 5×10^4 PFU dose). Continued treatment with F*Sj*RPI27 resulted in improved viral clearance and recovery of weight. However, lung samples still contained a mean 2.13 $\log_{10}$ viral titer on 6 dpi.

Interestingly, the strict prophylactic mode of action of F*Sj*RPI-27 was assessed by dosing mice 5×10^4 PFU/mouse of SARS-CoV-2 purified virus and providing F*Sj*RPI-27 at day 1 post-infection followed by additional doses at days 3, 5 and 7, which resulted in no difference from the virus-only cohort (data not shown). Thus, F*Sj*RPI-27 does not appear to function act as a potential therapeutic but does have strong prophylactic activity. In addition to antiviral activity, fucoidans are known to possess anti-inflammatory properties (Apostolova et al., 2020). Exploring the role of anti-inflammatory activity of F*Sj*RPI-27 warrants further investigation. It will be of interest in future studies to examine in greater detail the mechanism of F*Sj*RPI-27 mediated protection.

5. Conclusion

We demonstrated strong *in vitro* anti-SARS-CoV-2 properties of selected extracts of fucoidans and rhamnan sulfate. We also demonstrated strong *in vivo* antiviral activity of F*Sj*RPI-27 in a human ACE2 mouse model. The fucoidan extract is primarily comprised of high-molecular weight fucose-dominant and galactose-dominant polysaccharides and is highly acetylated at galactose unit. The rhamnan sulfate extract comprised of high-molecular weight sulfated rhamnan. Both high molecular weight sulfated polysaccharides showed extraordinary ability to bind the SARS-CoV-2 SGP *in vitro* based on SPR solution competition and pseudovirus cell entry assays. Enhanced survival and decreased viral burden after sub-lethal or lethal challenge of mice with pulmonary SARS CoV-2 indicated that mucosal inoculation of F*Sj*RPI27 can mediate substantial protection against COVID-19.

CRediT authorship contribution statement

Yuefan Song: Writing – original draft, Methodology, Investigation, Conceptualization. **Amit Singh:** Writing – review & editing, Writing – original draft, Methodology, Investigation. **Maisha M. Feroz:** Methodology, Investigation. **Shirley Xu:** Methodology, Investigation. **Fuming Zhang:** Methodology, Investigation. **Weihua Jin:** Resources. **Ambrish Kumar:** Formal analysis. **Parastoo Azadi:** Writing – review & editing, Funding acquisition, Formal analysis. **Dennis W. Metzger:** Writing – review & editing, Supervision, Project administration, Funding acquisition. **Robert J. Linhardt:** Supervision, Conceptualization. **Jonathan S. Dordick:** Writing – review & editing, Writing – original draft, Project administration, Funding acquisition, Conceptualization.

Declaration of competing interest

The authors declare the following financial interests/personal relationships which may be considered as potential competing interests: Jonathan S. Dordick reports financial support was provided by Rensselaer Polytechnic Institute. Robert Linhardt reports financial support was provided by Rensselaer Polytechnic Institute. Amit Singh reports financial support was provided by Albany Medical College. Dennis Metzger reports financial support was provided by Albany Medical

College. Jonathan S. Dordick reports a relationship with Lavaage, Inc. that includes: equity or stocks. Jonathan S. Dordick has patent #Compositions incorporating sulfated polysaccharides for inhibiting SARS-CoV-2 pending to Rensselaer Polytechnic Institute. Robert J. Linhardt has patent #Compositions incorporating sulfated polysaccharides for inhibiting SARS-CoV-2 pending to Rensselaer Polytechnic Institute. Weihua Jin has patent #Compositions incorporating sulfated polysaccharides for inhibiting SARS-CoV-2 pending to Rensselaer Polytechnic Institute. Fuming Zhang has patent #Compositions incorporating sulfated polysaccharides for inhibiting SARS-CoV-2 pending to Rensselaer Polytechnic Institute. Jonathan S. Dordick has patent #SYSTEMS AND METHODS UTILIZING *IN VIVO* EFFECTIVE SULFATED GLYCANS FOR COVID-19 PREVENTION AND TREATMENT pending to Rensselaer Polytechnic Institute. Amit Singh has patent #SYSTEMS AND METHODS UTILIZING *IN VIVO* EFFECTIVE SULFATED GLYCANS FOR COVID-19 PREVENTION AND TREATMENT pending to Albany Medical College. Dennis Metzger has patent #SYSTEMS AND METHODS UTILIZING *IN VIVO* EFFECTIVE SULFATED GLYCANS FOR COVID-19 PREVENTION AND TREATMENT pending to Albany Medical College. Jonathan S. Dordick is cofounder of Lavaage, Inc., which may license the disclosed patents from Rensselaer Polytechnic Institute. If there are other authors, they declare that they have no known competing financial interests or personal relationships that could have appeared to influence the work reported in this paper.

Data availability

Data will be made available on request.

Acknowledgments

This work was supported by grants from GlycoMIP (a National Science Foundation Materials Innovation Platform funded through Cooperative Agreement DMR-1933525), the New York State Biodefense Commercialization Fund, NIH (S10OD028523, R21AI156573), and the Department of Energy, Office of Science, Basic Energy Sciences, Chemical Sciences, Geosciences and Biosciences Division, under award #DE-SC0015662.

Appendix A. Supplementary data

Supplementary data to this article can be found online at https://doi.org/10.1016/j.carbpol.2024.122156.

References

Ale, M. T., Mikkelsen, J. D., & Meyer, A. S. (2011). Important determinants for fucoidan bioactivity: A critical review of structure-function relations and extraction methods for fucose-containing sulfated polysaccharides from brown seaweeds. *Marine Drugs, 9*(10), 2106–2130. https://doi.org/10.3390/md9102106

Álvarez-Viñas, M., Souto, S., Flórez-Fernández, N., Torres, M. D., Bandín, I., & Domínguez, H. (2021). Antiviral activity of carrageenans and processing implications. *Marine Drugs, 19*(8). https://doi.org/10.3390/md19080437

Apostolova, E., Lukova, P., Baldzhieva, A., Katsarov, P., Nikolova, M., Iliev, I., Peychev, L., Trica, B., Oancea, F., & Delattre, C. (2020). Immunomodulatory and anti-inflammatory effects of fucoidan: A review. *Polymers, 12*(10), 2338. https://doi.org/10.3390/polym12102338

Beaumont, M., Tran, R., Vera, G., Niedrist, D., Rousset, A., Pierre, R., … Forget, A. (2021). Hydrogel-forming algae polysaccharides: From seaweed to biomedical applications. *Biomacromolecules, 22*(3), 1027–1052. https://doi.org/10.1021/acs.biomac.0c01406

Bermejo-Jambrina, M., Eder, J., Kaptein, T. M., van Hamme, J. L., Helgers, L. C., Vlaming, K. E., … Geijtenbeek, T. B. H. (2021). Infection and transmission of SARS-CoV-2 depend on heparan sulfate proteoglycans. *The EMBO Journal, 40*(20), Article e106765. https://doi.org/10.15252/embj.2020106765

Bilan, M. I., Grachev, A. A., Shashkov, A. S., Nifantiev, N. E., & Usov, A. I. (2006). Structure of a fucoidan from the brown seaweed Fucus serratus L. *Carbohydrate Research, 341*(2), 238–245. https://doi.org/10.1016/j.carres.2005.11.009

Bilan, M. I., Grachev, A. A., Ustuzhanina, N. E., Shashkov, A. S., Nifantiev, N. E., & Usov, A. I. (2004). A highly regular fraction of a fucoidan from the brown seaweed Fucus distichus L. *Carbohydrate Research, 339*(3), 511–517. https://doi.org/10.1016/j.carres.2003.10.028

Bligh, M., Nguyen, N., Buck-Wiese, H., Vidal-Melgosa, S., & Hehemann, J.-H. (2022). Structures and functions of algal glycans shape their capacity to sequester carbon in the ocean. *Current Opinion in Chemical Biology, 71*, Article 102204. https://doi.org/10.1016/j.cbpa.2022.102204

Bruhn, A., Janicek, T., Manns, D., Nielsen, M. M., Balsby, T. J. S., Meyer, A. S., … Bjerre, A. B. (2017). Crude fucoidan content in two North Atlantic kelp species, Saccharina latissima and Laminaria digitata—Seasonal variation and impact of environmental factors. *Journal of Applied Phycology, 29*(6), 3121–3137. https://doi.org/10.1007/s10811-017-1204-5

Cao, L.-M., Sun, Z.-X., Makale, E. C., Du, G.-K., Long, W.-F., & Huang, H.-R. (2021). Antitumor activity of fucoidan: A systematic review and meta-analysis. *Translational Cancer Research, 10*(12), 5390. https://doi.org/10.21037/tcr-21-1733

Chi, Y., Jiang, Y., Wang, Z., Nie, X., & Luo, S. (2023). Preparation, structures, and biological functions of rhamnan sulfate from green seaweed of the genus Monostroma: A review. *International Journal of Biological Macromolecules, 249*, Article 125964. https://doi.org/10.1016/j.ijbiomac.2023.125964

Clausen, T. M., Sandoval, D. R., Spliid, C. B., Pihl, J., Perrett, H. R., Painter, C. D., … Esko, J. D. (2020). SARS-CoV-2 infection depends on cellular heparan sulfate and ACE2. *Cell, 183*(4), 1043–1057.e15. https://doi.org/10.1016/j.cell.2020.09.033

Clément, M. J., Tissot, B., Chevolot, L., Adjadj, E., Du, Y., Curmi, P. A., & Daniel, R. (2010). NMR characterization and molecular modeling of fucoidan showing the importance of oligosaccharide branching in its anticomplementary activity. *Glycobiology, 20*(7), 883–894. https://doi.org/10.1093/glycob/cwq046

Duarte, M. E. R., Cardoso, M. A., Noseda, M. D., & Cerezo, A. S. (2001). Structural studies on fucoidans from the brown seaweed Sargassum stenophyllum. *Carbohydrate Research, 333*(4), 281–293. https://doi.org/10.1016/s0008-6215(01)00149-5

Gelbach, A. L., Zhang, F., Kwon, S. J., Bates, J. T., Farmer, A. P., Dordick, J. S., … Linhardt, R. J. (2022). Interactions between heparin and SARS-CoV-2 spike glycoprotein RBD from omicron and other variants. *Frontiers in Molecular Biosciences, 9*, Article 912887. https://doi.org/10.3389/fmolb.2022.912887

Hanisch, F.-G. (2023). Revised structure model of norovirus-binding fucoidan from Undaria pinnatifida: Oligofucose chains branch off from a β6-galactane. *Glycobiology, 33*(7), 556–566. https://doi.org/10.1093/glycob/cwad039

Heiss, C., Black, I., Ishihara, M., Tatli, M., Devarenne, T. P., & Azadi, P. (2021). Structure of the polysaccharide sheath from the B race of the green microalga Botryococcus braunii. *Algal Research, 55*, Article 102252. https://doi.org/10.1016/j.algal.2021.102252

Kamhi, E., Joo, E. J., Dordick, J. S., & Linhardt, R. J. (2013). Glycosaminoglycans in infectious disease. *Biological Reviews, 88*(4), 928–943. https://doi.org/10.1111/brv.12034

Kim, S. Y., Jin, W., Sood, A., Montgomery, D. W., Grant, O. C., Fuster, M. M., … Linhardt, R. J. (2020). Characterization of heparin and severe acute respiratory syndrome-related coronavirus 2 (SARS-CoV-2) spike glycoprotein binding interactions. *Antiviral Research, 181*, Article 104873. https://doi.org/10.1016/j.antiviral.2020.104873

Kopplin, G., Rokstad, A. M., Mélida, H., Bulone, V., Skjåk-Bræk, G., & Aachmann, F. L. (2018). Structural characterization of fucoidan from Laminaria hyperborea: Assessment of coagulation and inflammatory properties and their structure-function relationship. *ACS Applied Bio Materials, 1*(6), 1880–1892. https://doi.org/10.1021/acsabm.8b00436

Kwon, P. S., Oh, H., Kwon, S. J., Jin, W., Zhang, F., Fraser, K., … Dordick, J. S. (2020). Sulfated polysaccharides effectively inhibit SARS-CoV-2 in vitro. *Cell Discovery, 6*(1), 50. https://doi.org/10.1038/s41421-020-00192-8

Kwon, P. S., Xu, S., Oh, H., Kwon, S. J., Rodrigues, A. L., Feroz, M., … Dordick, J. S. (2023). Suramin binds and inhibits infection of SARS-CoV-2 through both spike protein-heparan sulfate and ACE2 receptor interactions. *Communications Biology, 6*(1), 387. https://doi.org/10.1038/s42003-023-04789-z

Lahrsen, E., Schoenfeld, A. K., & Alban, S. (2019). Degradation of eight sulfated polysaccharides extracted from red and brown algae and its impact on structure and pharmacological activities. *ACS Biomaterials Science and Engineering, 5*(3), 1200–1214. https://doi.org/10.1021/acsbiomaterials.8b01113

Lee, J. B., Koizumi, S., Hayashi, K., & Hayashi, T. (2010). Structure of rhamnan sulfate from the green alga Monostroma nitidum and its anti-herpetic effect. *Carbohydrate Polymers, 81*(3), 572–577. https://doi.org/10.1016/j.carbpol.2010.03.014

Liu, L., Chopra, P., Li, X., Bouwman, K. M., Tompkins, S. M., Wolfert, M. A., … Boons, G. J. (2021). Heparan sulfate proteoglycans as attachment factor for SARS-CoV-2. *ACS Central Science, 7*(6), 1009–1018. https://doi.org/10.1021/acscentsci.1c00010

Luthuli, S., Wu, S., Cheng, Y., Zheng, X., Wu, M., & Tong, H. (2019). Therapeutic effects of fucoidan: A review on recent studies. *Marine Drugs, 17*(9), 487. https://doi.org/10.3390/md17090487

Oliveira, C., Neves, N. M., Reis, R. L., Martins, A., & Silva, T. H. (2020). A review on fucoidan antitumor strategies: From a biological active agent to a structural component of fucoidan-based systems. *Carbohydrate Polymers, 239*, Article 116131. https://doi.org/10.1016/j.carbpol.2020.116131

Peng, Y., Wang, Y., Wang, Q., Luo, X., He, Y., & Song, Y. (2018). Hypolipidemic effects of sulfated fucoidan from Kjellmaniella crassifolia through modulating the cholesterol and aliphatic metabolic pathways. *Journal of Functional Foods, 51*, 8–15. https://doi.org/10.1016/j.jff.2018.10.013

Pradhan, B., Nayak, R., Patra, S., Bhuyan, P. P., Behera, P. K., Mandal, A. K., … MubarakAli, D. (2022). A state-of-the-art review on fucoidan as an antiviral agent to combat viral infections. *Carbohydrate Polymers, 291*, 119551. https://doi.org/10.1016/j.carbpol.2022.119551

Ray, B., Ali, I., Jana, S., Mukherjee, S., Pal, S., Ray, S., Schütz, M., & Marschall, M. (2022). Antiviral strategies using natural source-derived sulfated polysaccharides in

the light of the COVID-19 pandemic and major human pathogenic viruses. *Viruses, 14*(1), 35. https://doi.org/10.3390/v14010035
Salih, A. E. M., Thissera, B., Yaseen, M., Hassane, A. S. I., El-seedi, H. R., Sayed, A. M., & Rateb, M. E. (2021). Marine sulfated polysaccharides as promising antiviral agents: A comprehensive report and modeling study focusing on Sars CoV-2. *Marine Drugs, 19*(8), 406. https://doi.org/10.3390/md19080406
Shi, D., Bu, C., He, P., Song, Y., Dordick, J. S., Linhardt, R. J., … Zhang, F. (2022). Structural characteristics of heparin binding to SARS-CoV-2 spike protein RBD of omicron sub-lineages BA.2.12.1, BA.4 and BA.5. *Viruses, 14*(12), 2606. https://doi.org/10.3390/v14122696
Singh, A. K., Stellrecht, K. A., Arunachalam, T., Barman, T. K., Robek, M. D., Waxman, M. J., … Metzger, D. W. (2021). Lack of active SARS-CoV-2 virus in a subset of PCR-positive COVID-19 congregate care patients. *Journal of Clinical Virology, 141*, Article 104879. https://doi.org/10.1016/j.jcv.2021.104879
Song, Y., Wang, Q., He, Y., Ren, D., Kow, F., Li, J., Liu, S., & Cong, H. (2017). The positive effects of fucoidans extracted from the brown seaweed Saccharina japonica on protection against CCl4-induced liver injury. *Journal of Applied Phycology, 29*(4), 2077–2087. https://doi.org/10.1007/s10811-017-1097-3
Song, Y., Wang, Q., Wang, Q., He, Y., Ren, D., Liu, S., & Wu, L. (2018). Structural characterization and antitumor effects of fucoidans from brown algae Kjellmaniella crassifolia farmed in northern China. *International Journal of Biological Macromolecules, 119*, 125–133. https://doi.org/10.1016/j.ijbiomac.2018.07.126
Song, Y., He, P., Rodrigues, A. L., Datta, P., Tandon, R., Bates, J. T., … Linhardt, R. J. (2021). Anti-SARS-CoV-2 activity of rhamnan sulfate from Monostroma nitidum. *Marine drugs, 19*(12), 685. https://doi.org/10.3390/md19120685
Sterner, M., & Gröndahl, F. (2021). Extraction of laminarin from Saccharina latissima seaweed using cross-flow filtration. *Journal of Applied Phycology, 33*, 1825–1844. https://doi.org/10.1007/s10811-021-02398-z/Published
Stiger-Pouvreau, V., Bourgougnon, N., & Deslandes, E. (2016). Carbohydrates from seaweeds. In *Seaweed in health and disease prevention* (pp. 223–274). Elsevier Inc.. https://doi.org/10.1016/B978-0-12-802772-1.00008-7
Sun, L., Chopra, P., Tomris, I., van der Woude, R., Liu, L., de Vries, R. P., & Boons, G. J. (2023). Well-defined heparin mimetics can inhibit binding of the trimeric spike of SARS-CoV-2 in a length-dependent manner. *JACS Au, 3*(4), 1185–1195. https://doi.org/10.1021/jacsau.3c00042
Sun, X., Ai, C., Wen, C., Peng, H., Yang, J., Cui, Y., & Song, S. (2023). Inhibitory effects of fucoidan from Laminaria japonica against some pathogenic bacteria and SARS-CoV-2 depend on its large molecular weight. *International Journal of Biological Macromolecules, 229*, 413–421. https://doi.org/10.1016/j.ijbiomac.2022.12.307
Taneja, R. (2021). Current status of oral pentosan polysulphate in bladder pain syndrome/interstitial cystitis. *International Urogynecology Journal, 32*(5), 1107–1115. https://doi.org/10.1007/s00192-020-04517-9
Wang, S., Wang, W., Hou, L., Qin, L., He, M., Li, W., & Mao, W. (2020). A sulfated glucuronorhamnan from the green seaweed Monostroma nitidum: Characteristics of its structure and antiviral activity. *Carbohydrate Polymers, 227*, Article 115280. https://doi.org/10.1016/j.carbpol.2019.115280
Wang, S. H., Huang, C. Y., Chen, C. Y., Chang, C. C., Huang, C. Y., Di Dong, C., & Chang, J. S. (2020). Structure and biological activity analysis of fucoidan isolated from Sargassum siliquosum. *ACS Omega, 5*(50), 32447–32455. https://doi.org/10.1021/acsomega.0c04591
Xu, G., Amicucci, M. J., Cheng, Z., Galermo, A. G., & Lebrilla, C. B. (2018). Revisiting monosaccharide analysis-quantitation of a comprehensive set of monosaccharides using dynamic multiple reaction monitoring. *Analyst, 143*(1), 200–207. https://doi.org/10.1039/c7an01530e
Yao, Y., & Yim, E. K. F. (2021). Fucoidan for cardiovascular application and the factors mediating its activities. *Carbohydrate Polymers, 270*, Article 118347. https://doi.org/10.1016/j.carbpol.2021.118347
Yu, X. A., McLean, C., Hehemann, J. H., Angeles-Albores, D., Wu, F., Muszyński, A., … Polz, M. F. (2024). Low-level resource partitioning supports coexistence among functionally redundant bacteria during successional dynamics. *The ISME Journal, 18*(1), Article wrad013. https://doi.org/10.1093/ismejo/wrad013
Yue, J., Jin, W., Yang, H., Faulkner, J., Song, X., Qiu, H., … Wang, L. (2021). Heparan sulfate facilitates spike protein-mediated SARS-CoV-2 host cell invasion and contributes to increased infection of SARS-CoV-2 G614 mutant and in lung cancer. *Frontiers in Molecular Biosciences, 8*, Article 649575. https://doi.org/10.3389/fmolb.2021.649575
Yuguchi, Y., Ly, B. M., Van Nguyen, B., Van, T. T. T., & Thuy, T. T. T. (2016). Study on branched structure–physiological activity relationship of fucoidan. *Chemistry Letters, 45*(7), 840–842. https://doi.org/10.1246/cl.160189
Zhang, Q., Chen, C. Z., Swaroop, M., Xu, M., Wang, L., Lee, J., … Ye, Y. (2020). Heparan sulfate assists SARS-CoV-2 in cell entry and can be targeted by approved drugs in vitro. *Cell Discovery, 6*(1), 80. https://doi.org/10.1038/s41421-020-00222-5